3D-Coherent anti-Stokes Raman scattering Fourier ptychography tomography (CARS-FPT)

Sandro Heuke, Hervé Rigneault, Anne Sentenac

3D-Coherent anti-Stokes Raman scattering Fourier ptychography tomography (CARS-FPT)

SANDRO HEUKE[1,2], HERVÉ RIGNEAULT[1,2,*] AND ANNE SENTENAC[1,3,*]

[1]*Aix Marseille Univ, CNRS, Centrale Marseille, Turing Center for Living Systems, Institut Fresnel, Marseille, France.*
[2]*Team MOSAIC*
[3]*Team SEMO*
[*]*Corresponding authors: herve.rigneault@fresnel.fr, anne.sentenac@fresnel.fr*

Abstract: Fourier ptychography tomography (FPT) is a novel computational technique for coherent imaging in which the sample is numerically reconstructed from images acquired under various illumination directions. FPT is able to provide three-dimensional (3D) reconstructions of the complex sample permittivity with an increased resolution compared to standard microscopy. In this work, FPT is applied to Coherent anti-Stokes Raman scattering (CARS) imaging. We show on synthetic data that complex third-order susceptibilities can be reconstructed in 3D from a limited number of widefield CARS images. In addition, we observe that the non-linear interaction increases significantly the potential of CARS-FPT compared to linear FPT in terms of resolution. In particular, with a careful choice of the pump and Stokes beam directions, CARS-FPT is able to provide optical sectioning even in transmission configuration.

1. Introduction

Fourier ptychography (FP) is a versatile technique with great potential for research and industrial applications [1]. It consists in reconstructing numerically the sample from multiple images recorded under different orientations of a collimated beam [2]. Relevant for all coherent imaging techniques, FP was first developed in the domain of optical microscopy but soon extended to X-ray [3] and near infra-red [4] imaging. It appeared as a simple approach for improving the lateral resolution [2, 5], or more precisely the space-bandwidth product (SBP) of the imager and, most importantly could image both phase and absorptive objects [6]. Furthermore, it can be used to estimate the aberrations of imaging systems [7].

1.1. Fourier Ptychography Tomography for coherent linear imaging

Recently, it was shown that, provided enough illumination angles were used, FP can also reconstruct the sample in three-dimensions [8–14]. The 3D resolution of Fourier Ptychography Tomography (FPT) can be analysed in the same way as that of Optical Diffraction Tomography (ODT) ([15, 16]). Under the weak scattering or Born approximation, when the sample is illuminated by a plane wave with wavevector $\mathbf{k}_{ex}$, the image recorded on the camera depends on the 3D Fourier transform of the sample permittivity $\tilde{\epsilon}(\mathbf{K})$ where the support of $\mathbf{K}$ is a shifted cap of sphere [17] defined by

$$\mathbf{K} = \mathbf{k}_{out} - \mathbf{k}_{ex} \tag{1}$$

where $\mathbf{k}_{out} = \mathbf{k}_{||} + k_z\hat{\mathbf{z}}$ and $k_z = \sqrt{k_{ex}^2 - k_{||}^2}$ corresponds to the wavevector of the diffracted field that is collected by the microscope objective of Numerical Aperture NA and satisfy, $k_{||} < k_{ex}$NA. Here, k_z represents the projection of $\mathbf{k}_{out}$ along the optical axis (z-axis) oriented from the sample to the objective and $\mathbf{k}_{||}$ is the projection of $\mathbf{k}_{out}$ on the plane normal to the optical axis. Thus, whatever the reconstruction procedure (as long as Born approximation is valid

and no regularization is used), one cannot expect to recover sample information beyond the Fourier domain composed of the unions of the shifted caps of sphere provided by the successive illuminations. In the standard transmission configuration, where the illumination sources and the observation detectors are placed on either side of the sample, the Fourier components of the sample along the optical axis are impossible to recover - see Fig. 1 [1, 8]. This issue, also known as the missing cone problem prevents FPT and ODT techniques (as well as classical widefield microscopes) from providing 3D reconstructions of multilayered samples such as the superposition of elongated cells. By contrast, FPT and ODT techniques in reflection configuration (as well as the more classical Optical Coherence Tomography [10, 18, 19]), in which the sources and detectors are placed on the same side of the sample, are able to visualize the interfaces of multilayered media. But, in this case, they miss the low frequencies of the samples and cannot recover the smooth variations of the permittivity [20]. This incomplete probing of the Fourier space imposed by the illumination and detection positions is the fundamental limit of 3D widefield linear imaging in general and FPT in particular.

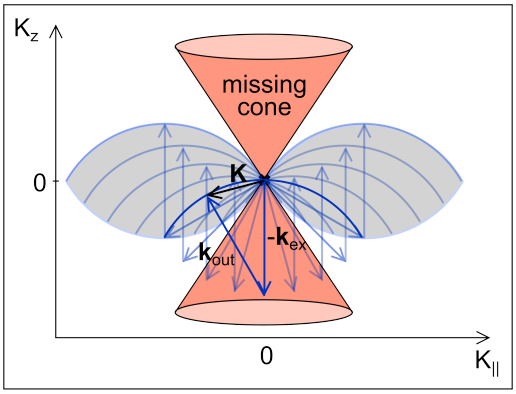

Fig. 1. Accessible sample spatial frequencies (K-support) of a linear FPT experiment, defined by $\mathbf{K} = \mathbf{k}_{\text{out}} - \mathbf{k}_{\text{ex}}$. Note that the gray double-lobe is just a (x-z) section of the doughnut-like sample support. No information is obtained from the area marked in red. This area represents the missing cone and is responsible for the lack of optical sectioning of widefield microscopy, FPT and ODT in transmission configuration

1.2. Fourier Ptychography Tomography for coherent non-linear imaging

FPT's ability to recover in 3D the real and imaginary part of the sample parameter from a limited number of intensity images appears to be particularly interesting for CARS imaging. The latter is a unique marker-free imaging approach able to provide a chemical characterization of the sample thanks to a non-linear light-matter interaction. The CARS radiation is linked to the sample by the non-linear third-order susceptibility tensor, $\chi^{(3)}_{aS}$, the imaginary part of which is proportional to the concentration of Raman active molecular groups (equivalent to linear Raman) while its real part accounts for a vibrational contribution plus a non resonant electronic contribution [21]. For chemical quantification, an ideal CARS imaging technique should be able to recover both the amplitude and phase of $\chi^{(3)}_{aS}$ in order to separate the useful signal $\chi^{(3)}_{aS,im}$ from the background non-resonant one, $\chi^{(3)}_{aS,re}$. Now, CARS microscopy is usually based on point-scanning techniques and is sensitive only to the square of the amplitude of $\chi^{(3)}_{aS}$. The coupling of FPT to CARS is thus expected to improve the sample information given by this non-linear imaging approach. We have recently modeled the image obtained in CARS-FPT [22] and shown that it depends on the 3D Fourier transform of the third-order susceptibility $\tilde{\chi}^{(3)}_{aS}(\mathbf{K})$ where the K-support in the Fourier

space is a shifted cap of sphere defined by,

$$\mathbf{K} = \mathbf{k}_{aS} + \mathbf{k}_S - \mathbf{k}_{p1} - \mathbf{k}_{p2} \tag{2}$$

with $\mathbf{k}_{aS}$ denoting the wavevector of the radiated anti-Stokes radiation that is collected by the microscope objective, $k_{aS||} < \frac{\omega_{aS}}{c}\text{NA}$. $\mathbf{k}_S$ is the wavevector of the Stokes beam and $\mathbf{k}_{p1}$ and $\mathbf{k}_{p2}$ are the wavevectors of the probe and pump beams respectively, with $\omega_{aS} = \omega_{p1} + \omega_{p2} - \omega_S$ (note that in degenerate CARS, the same beam is used for pumping and probing, $\mathbf{k}_{p1} = \mathbf{k}_{p2}$). Figure 2 outlines the accessible K-supports using various angle scanning for the probe, pump and Stokes beams (while remaining in a classical transmission configuration). Note that some of these illumination schemes have already been implemented experimentally [23–26] but without changing the angles.

If the incident angles of the pump, probe and Stokes beam are set equal and changed simultaneously, the missing cone problem persists as evident from Fig. 2 a. Here, the accessible sample K-support is the same as that obtained in the linear scattering case, assuming equal refractive indices for all wavelengths. Yet, by keeping the Stokes or pump+probe beam fixed along the optical axis (K_z) and angle-scanning the other, it is already possible to access sample spatial frequencies along the optical axis, thus removing the missing cone (Figs. 2 b,c). To address larger ranges of K_z at least two scanners controlling the incident angles are required. Scanning the pump ($\mathbf{k}_{p1}$) and probe ($\mathbf{k}_{p2}$) wave-vectors in a mirrored fashion probes $K_z > 0$ (Fig. 2 d) while changing the angle of the Stokes wave-vector ($\mathbf{k}_S$) in line with the angle of co-propagating pump ($\mathbf{k}_{p1}$) and probe ($\mathbf{k}_{p2}$) wave-vectors yields access to $K_z < 0$ (Fig. 2 d). Yet, to obtain information on both $\tilde{\chi}^{(3)}_{aS}(\mathbf{K})$ and $\tilde{\chi}^{(3)}_{aS}(-\mathbf{K})$, which is mandatory for recovering the imaginary and real part of the non-linear susceptibility, one should favor the 3 beam scanning scheme outlined in Fig. 2 f. For this reason, we consider in the following only the scanning scheme Fig. 2 f where CARS radiation is collected in transmission configuration and the pump, probe and Stokes wave-vectors can be controlled independently so that the K-support of accessible sample frequencies is a convex 3D domain centered about the null frequency. We demonstrate on synthetic data the potential of this approach for reconstructing in 3D the complex non-linear susceptibility of the sample from a limited number of widefield CARS images.

2. Designing a CARS-FPT experiment

For the purpose of illustration, we consider the hypothetical experimental configuration presented in Fig. 3. Here, a pulsed laser source generates the Stokes (S) beam but also pumps an optical parametric amplifier (OPA) that emits two beams of independently tunable wavelength serving as pump (p1) and probe (p2) to drive the CARS process. To distinguish 3-color from 2-color (degenerative) CARS, the wavelength of the beams are selected so that the anti-Stokes radiation is readily separated by dielectric filters. The 3 excitation beams are angle-tuned independently using 3 laser scanning mirrors (see Fig. 3) while the anti-Stokes radiation is collected by an objective lens in a 4f-configuration. In the following, the pump, probe and Stokes wavelengths were set to 797 nm, 730 nm and 1030 nm, respectively, resulting in an anti-Stokes radiation at 600 nm and the objective numerical aperture was set to NA = 0.2.

The optimization of the illumination angles is an important step of the experiment design as it determines the final 3D resolution and the maximal thickness of the sample under study. Here, we wanted the accessible K-support, made of the union of shifted caps of sphere defined by Eq. (2), to be close to a cube centered about the null frequency with width about $0.3k_{aS}$ yielding an ideal 3D resolution about 2 microns (with a CARS radiation at 0.6 microns). In addition, the axial sampling of the cube had to be small enough to be able to image 100 microns thick samples. Last, there must be enough redundancy in the Fourier information of the successive images for the FPT reconstruction algorithm to succeed [22]. To meet these requirements, we approximated the cap of sphere to a disk of diameter $\text{NA}k_{aS}$ and we searched the angles of the probe, pump and Stokes

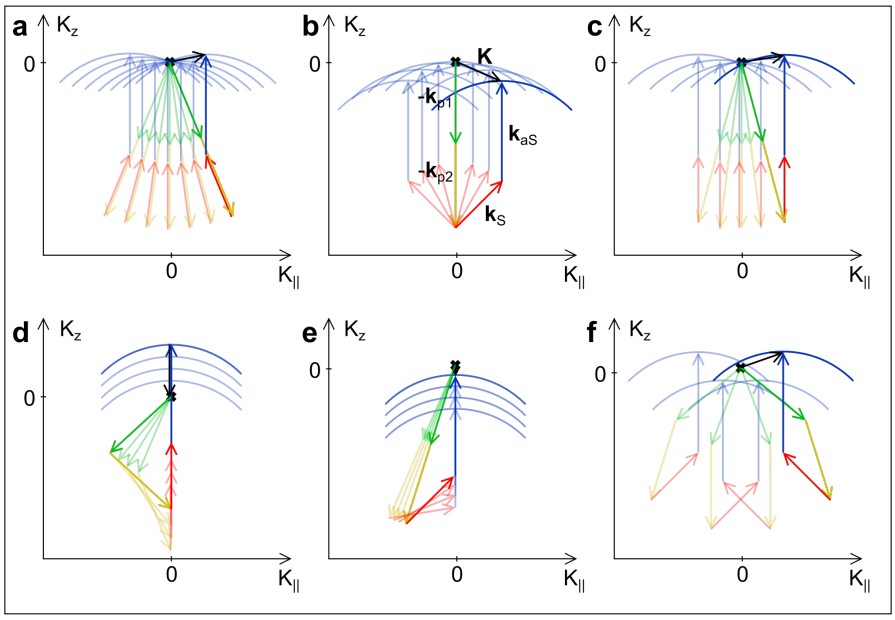

Fig. 2. Accessible sample spatial frequencies (K-support) of CARS-FTP for different illumination configurations. The pump wavevector is $\mathbf{k}_{p1}$ (green), the probe $\mathbf{k}_{p2}$ (yellow), the Stokes $\mathbf{k}_S$ (red). The maximum solid angle of the collected anti-Stokes wavevectors collected, $\mathbf{k}_{aS}$ (dark blue & pointing to a cap of a sphere), is set by the NA of the microscope objective. One scanner a-c; two scanners: d-e; three scanners: f. The three-scanners configuration allows the probing of a convex K-support about the null frequency, thus providing both optical sectioning and sensitivity to smoothly varying samples.

beams such that the centers of the shifted disks were placed at $(k_x, k_y, k_z) = (n\Delta k, m\Delta k, p\Delta k_z)$ with $\Delta k = 0.05 k_{aS}$, $\Delta k_z = 0.006 k_{aS}$ and $(m, n, p) \in (-1, 0, 1) \times (-1, 0, 1) \times (-20..., 0, ..., 20)$. These values ensured that the cube was approximately filled with the shifted caps of sphere with the appropriate sampling, as illustrated in Fig. (3). To obtain the polar and azimuthal angles of the probe, pump and Stokes beams, we solved numerically the non-linear under-determined system,

$$\begin{pmatrix} n\Delta k \\ m\Delta k \\ p\Delta k_z \end{pmatrix} = \begin{pmatrix} k_S \sin\theta_S - k_{p1} \sin\theta_{p1} \cos\phi_{p1} - k_{p2} \sin\theta_{p2} \cos\phi_{p2} \\ -k_{p1} \sin\theta_{p1} \sin\phi_{p1} - k_{p2} \sin\theta_{p2} \sin\phi_{p2} \\ k_{aS} - k_{p1} \cos\theta_{p1} - k_{p2} \cos\theta_{p2} + k_S \cos\theta_S \end{pmatrix} \tag{3}$$

where ϕ_S was fixed to 0.

Once the $L = 3 \times 3 \times 41$ angles of illumination were found, we simulated CARS-FPT images for various samples.

3. Simulating CARS-FPT images

We recall here the main steps of the model linking the CARS-FPT images to the sample non-linear susceptibility tensor, $\overleftrightarrow{\chi}^{(3)}_{aS}(\mathbf{r})$, where $\mathbf{r} = (\mathbf{r}_{||}, z)$ is a point of the 3D space.

Assuming that the light entering the objective lens is x-polarized, the incident electric fields in the sample are modeled by,

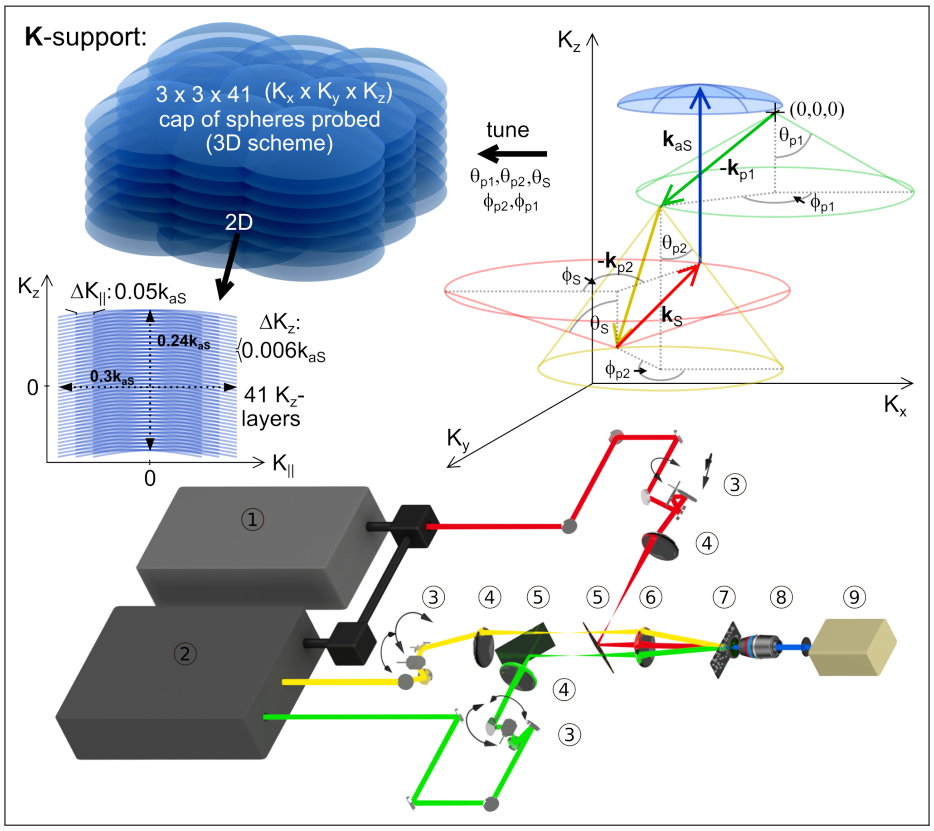

Fig. 3. Prospective experimental setup: 1 pulsed pump laser source, 2 optical parametric amplifier (OPA) with a two-color output, 3 laser scanning mirrors, 4 scan lenses, 5 dichroic beam combiner, 6 objective lens, 7 sample, 8 4f-CARS radiation collection system with x-polarizer, 9 camera. The top scheme reproduces Fig. 2f in 3D and highlights the used variables. The illumination angles are chosen so that the sample accessible spatial frequencies (K-support) is a convex cuboid domain centered about the null frequency (corresponding to the stack of blue caps of spheres).

$$\mathbf{E}_q(\mathbf{r},\phi_q,\theta_q) = E_0\sqrt{n_q\cos\theta_q}\begin{bmatrix}\cos^2\phi_q\cos\theta_q+\sin^2\phi_q\\-(1-\cos\theta_q)\sin\phi_q\cos\phi_q\\-\sin\theta_q\cos\phi_q\end{bmatrix}\exp\left[i\mathbf{k}_q\cdot\mathbf{r}\right], \tag{4}$$

where q stands for either p1, p2 or S and n_q is the refractive index which is set to 1 for all wavelengths.

The anti-Stokes field at point $\mathbf{R} = (\mathbf{R}_{||}, 0)$ of the detection plane of the 4f imaging system is given by the field radiated by the anti-Stokes polarization density induced by the non-linear interaction,

$$\mathbf{P}^{(3)}_{aS}(\mathbf{r}) = \overleftrightarrow{\chi}^{(3)}_{aS}(\mathbf{r})\mathbf{E}_{p1}(\mathbf{r})\mathbf{E}_{p2}(\mathbf{r})\mathbf{E}^*_S(\mathbf{r}). \tag{5}$$

Introducing the microscope Green tensor $\overleftrightarrow{\mathbf{G}}$ such that $\overleftrightarrow{\mathbf{G}}(\mathbf{R},\mathbf{r}')\mathbf{p}$ is the field radiated at $\mathbf{R}$ by an electric dipole placed at $\mathbf{r}'$, the anti-Stokes field reads,

$$\mathbf{E}_{aS}(\mathbf{R}) = \int \overleftrightarrow{\mathbf{G}}(\mathbf{R}, \mathbf{r}')\mathbf{P}^{(3)}_{aS}(\mathbf{r}')\mathrm{d}\mathbf{r}'. \tag{6}$$

The Green tensor can be assimilated to the coherent point spread function of the microscope. The support of its 3D Fourier transform (or optical transfer function) is a cap of sphere of radius k_{aS} defined by $k_{||} < k_{aS}\mathrm{NA}$ and $k_z > 0$. In our model, the tensor $\overleftrightarrow{\mathbf{G}}$ accounts for the vectorial nature of the electric field and for the magnification of the microscope [22, 27].

The image model is given by

$$I(\mathbf{R}_{||}) = |\mathbf{E}_{aS}(\mathbf{R})|^2 \tag{7}$$

Hereafter, the 'measured' CARS-FPT images were simulated using Eq. (7) and deteriorated with Poisson noise, using a maximum of 10^4 photons for the brightest pixel.

4. Reconstructing the sample non-linear susceptibility from CARS-FPT images

To simplify the reconstruction procedure, we assumed that the orientation of the Raman scatterers within the sample is isotropic and only the x-component of the anti-Stokes electric field is detected while the pump, probe and Stokes electric fields may have (x, y, z) components depending on the incident angle (see Eq. 4). Thus, the non-zero tensor elements of the anti-Stokes susceptibility involved in the image formation are, $\overleftrightarrow{\chi}_{1111}$, $\overleftrightarrow{\chi}_{1122}$=$\overleftrightarrow{\chi}_{1133}$, $\overleftrightarrow{\chi}_{1212}$=$\overleftrightarrow{\chi}_{1313}$, $\overleftrightarrow{\chi}_{1221}$=$\overleftrightarrow{\chi}_{1331}$ and follow the relation $\overleftrightarrow{\chi}_{1111} = \overleftrightarrow{\chi}_{1122} + \overleftrightarrow{\chi}_{1221} + \overleftrightarrow{\chi}_{1212}$ [28]. We assume the relation between the tensor elements for a given molecular species to be known and set them to $1/3\overleftrightarrow{\chi}_{1111} = \overleftrightarrow{\chi}_{1122} = \overleftrightarrow{\chi}_{1221} = \overleftrightarrow{\chi}_{1212}$. Under these assumptions, the reconstruction procedure amounts to recover a complex scalar $N(\mathbf{r})$, whose imaginary part represents the density of Raman active molecular groups while the real part indicates the vibrational and electronic contribution, such that $\overleftrightarrow{\chi}^{(3)}_{aS}(\mathbf{r}) = N(\mathbf{r})\overleftrightarrow{\chi}^{,(3)}_{aS}$ where $\overleftrightarrow{\chi}^{,(3)}_{aS}$ is known. The inversion scheme consists in estimating N so as to minimize the distance F between the measured images and the image model,

$$F(N) \propto \sum_{l=1}^{L} \int |I_l^{\mathrm{mes}}(\mathbf{R}_{||}) - I_l(\mathbf{R}_{||})|^2 \mathrm{d}\mathbf{R}_{||} \tag{8}$$

where the subscript l indicates the illumination configuration, $l = 1, ..., L$ with $L = 3 \times 3 \times 41$ in our configuration. I_l^{mes} corresponds to the experimental images (here obtained numerically) and $I_l(N)$ is the simulated image obtained with the estimation of N. We define an investigating domain Ω beyond which N is assumed to be null. Ω is discretized into M voxels over which N is assumed to be constant.

The minimization of F is done using a gradient descent that is thoroughly described in [22]. Starting from a homogeneous initial guess, N is modified iteratively following,

$$N_m^n = N_m^{n-1} + \alpha g_m \tag{9}$$

where n indicates the iteration step, m one voxel of Ω and α is a real scalar. The gradient at voxel m, is obtained via the partial derivative,

$$\left.\frac{\partial F}{\partial N_m}\right|_{N^{n-1}_{i=1...M}} = \mathrm{Re}(g_m^*) \tag{10}$$

where $*$ indicates the complex conjugate. To avoid a too harsh correction at a single voxel level, we have capped g_m such that its amplitude does not exceed 10 times the median amplitude. At each iteration, α is adjusted to yield a steady decrease of F.

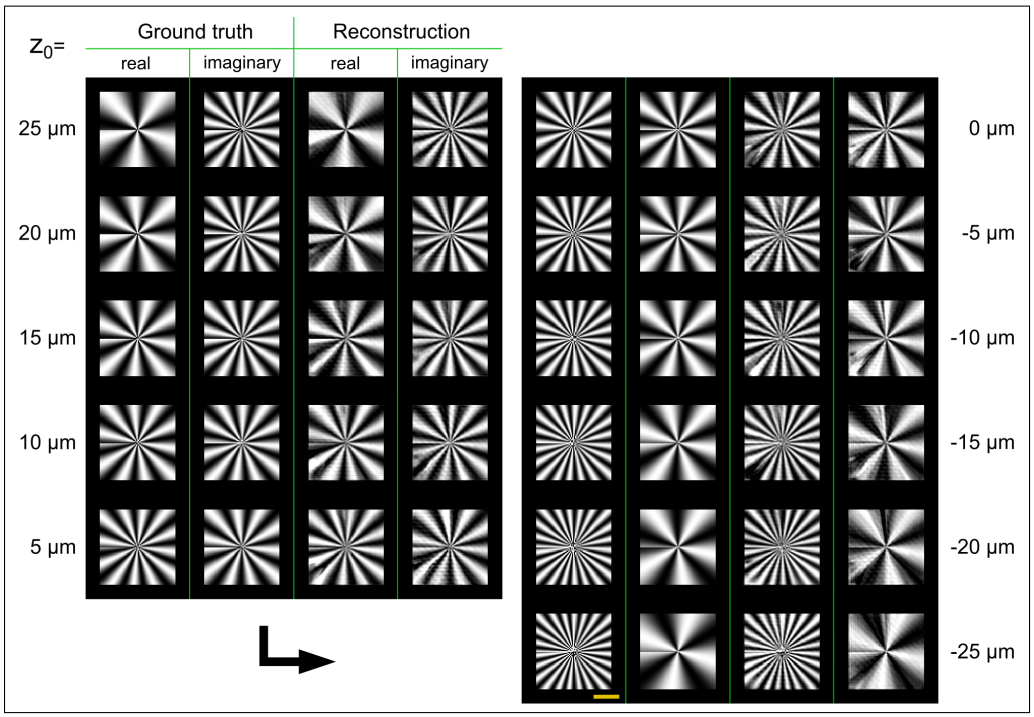

Fig. 4. Reconstruction of a sample made of 11 complex-valued layers. The blue scale bar is 50 µm. See also the movie, Visualization 1

5. Results

We first considered a 3D sample made of 11 superimposed layers of spoke patterns [29]. The sample is discretized over $101 \times 101 \times 11$ cuboid voxels with a lateral size of 2 microns and axial size 5 microns. The scatterer density is defined as as $N_{\text{true}}(\mathbf{r}_{||}, q\Delta z) = (1 + i + \cos[(1 + q/3)\pi\varphi + \pi/3] + i\cos[(8 - q/1.7)\pi\varphi + \pi/2])/2$ where φ is the angle between the x-axis and $\mathbf{r}_{||}$.

The inversion algorithm was started from a homogeneous initial guess $N^1(\mathbf{r}) = 0.01 + i0.01$ and the final reconstruction is shown in Fig. (4). It is seen that both the real and imaginary part of N are accurately recovered for each layer. Visualization 1, which displays the reconstruction update step by step for each layer, shows that the reconstruction progresses faster at positions where the gradient of N is important (at the edges). In contrast, the inversion algorithm has difficulty for recovering slowly varying N and can even fail to estimate homogeneous area. This behavior is easily explained by noting that when the sample is uniform, changing the illumination angles does not modify the image and consequently does not bring additional information.

This limit to CARS-FPT was particularly visible in another experiment where the sample was made of randomly placed large homogeneous beads. We observed (not shown) that the reconstruction algorithm was not able to estimate properly the scatterer density within the beads. It is worth noting that this issue is not encountered in classical linear FPT where the recorded intensity can be modeled as the interference pattern between the specular transmitted field and the field diffracted by the sample. Basically, linear FPT is equivalent to in line holography with various incident angles. The presence of a reference field significantly helps the recovering of the field phase and consequently of the sample complex permittivity. In CARS-FPT, unfortunately, there is no specular field with which the CARS radiation interferes. To improve the reconstruction, we have thus proposed to add a thin homogeneous non-linear layer below the sample to generate

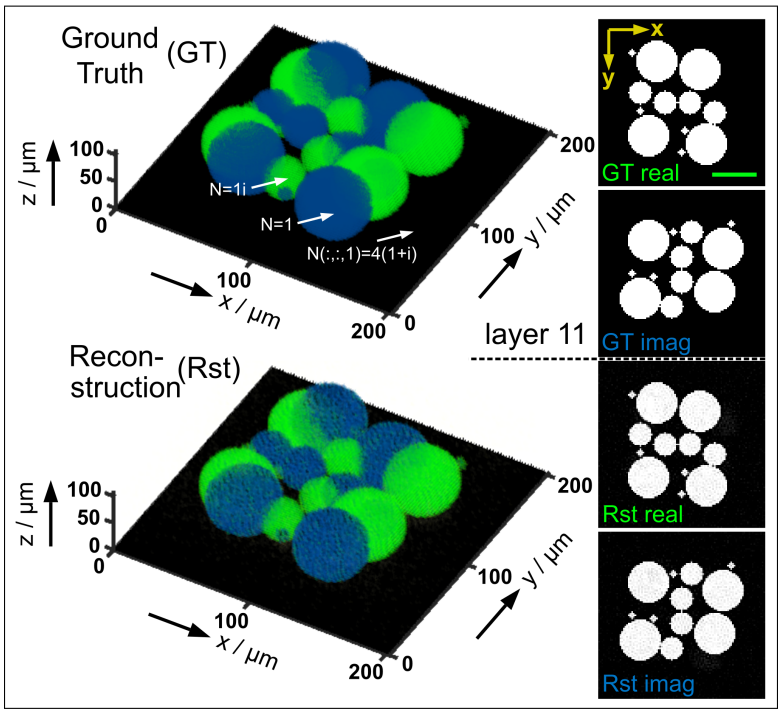

Fig. 5. Reconstruction of polymer beads on a $101 \times 101 \times 21$ cubic grid with mesh size 2 microns. The beads are homogeneous with $N_{\text{true}} = 1 + i$. A thin polymer layer with known thickness is added to generate a reference field $(N_{\text{layer}}) = 4 + i4$. The reconstruction of both the real and imaginary part of the beads is particularly accurate. The 2D plots on the right show a cut at the center of the sample. The scale bar is 40 µm.

a reference anti-Stokes CARS radiation. For a real-world experiment, this reference CARS field could come from the CARS non-resonant background of the sample holder and could be even amplified by covering the sample holder with a thin transparent polymer layer that would radiate a strong homogeneous resonant CARS reference signal. With this reference field, the reconstruction of the beads was remarkably accurate as shown in Fig. (5).

6. Conclusion

In this work we presented a numerical study of the performances of 3D coherent anti-Stokes Raman scattering Fourier ptychography tomography (CARS-FPT). We expect this widefield CARS imaging approach to be accessible in the near future with the commercially available dual-color fiber-laser/OPA combinations [22]. We showed that with a careful optimization of the angles of the pump, probe and Stokes beams, CARS-FPT has the potential to image the density of the active Raman molecular groups with an isotropic resolution in three-dimensions. It can provide true optical sectioning while being sensitive to smoothly varying samples, thus combining the advantages of transmission and reflection microscopy in a single objective configuration. Yet, the reconstruction procedure of CARS-FPT is not always successful, especially when the sample exhibits locally uniform domains. We observed that it worked significantly better if a reference CARS field was introduced to interfere with the sample radiation. Eventually, this reference field could come from the non-resonant or resonant background of the sample holder. Another foreseen problem is that CARS-FPT requires the knowledge of the illuminations (here

collimated beams). Uncontrolled incident phase distortions, possibly caused by the sample itself, may induce artifacts in the reconstruction. Using infra-red excitation wavelengths as well as refractive-index matched samples should reduce this issue. Despite these limitations, CARS-FPT seems a promising approach for widefield quantitative chemical characterization of samples in three-dimensions.

Disclosure

The authors declare no conflicts of interest.

Data availability

The data that support the findings of this study are available from the corresponding author upon reasonable request.

Funding Information

We acknowledge financial support from the Centre National de la Recherche Scientifique (CNRS), Aix-Marseille University (A-M-AAP-ID-17-13-170228-15.22-RIGNEAULT), A*Midex (ANR-11-IDEX-0001-02), Cancéropôle Provence-Alpes Côte d'Azur, French National Cancer institute (INCA), Région Sud, ANR grants (ANR-10-INSB-04-01, ANR-11-INSB-0006, ANR-16-CONV-0001), INSERM PC201508 and 18CP128-00.

References

1. P. C. Konda, L. Loetgering, K. C. Zhou, S. Xu, A. R. Harvey, and R. Horstmeyer, "Fourier ptychography: current applications and future promises," Opt. Express **28**, 9603 (2020).
2. G. Zheng, R. Horstmeyer, and C. Yang, "Wide-field, high-resolution fourier ptychographic microscopy," Nat. Photonics **7**, 739–745 (2013).
3. K. Wakonig, A. Diaz, A. Bonnin, M. Stampanoni, A. Bergamaschi, J. Ihli, M. Guizar-Sicairos, and A. Menzel, "X-ray fourier ptychography," Sci. Adv. **5**, eaav0282 (2019).
4. S. Sen, I. Ahmed, B. Aljubran, A. A. Bernussi, and L. G. de Peralta, "Fourier ptychographic microscopy using an infrared-emitting hemispherical digital condenser," Appl. Opt. **55**, 6421 (2016).
5. J. Sun, C. Zuo, L. Zhang, and Q. Chen, "Resolution-enhanced fourier ptychographic microscopy based on high-numerical-aperture illuminations," Sci. Reports **7** (2017).
6. X. Ou, R. Horstmeyer, C. Yang, and G. Zheng, "Quantitative phase imaging via fourier ptychographic microscopy," Opt. Lett. **38**, 4845 (2013).
7. J. Chung, J. Kim, X. Ou, R. Horstmeyer, and C. Yang, "Wide field-of-view fluorescence image deconvolution with aberration-estimation from fourier ptychography," Biomed. Opt. Express **7**, 352 (2016).
8. R. Horstmeyer, J. Chung, X. Ou, G. Zheng, and C. Yang, "Diffraction tomography with fourier ptychography," Optica **3**, 827 (2016).
9. R. Ling, W. Tahir, H.-Y. Lin, H. Lee, and L. Tian, "High-throughput intensity diffraction tomography with a computational microscope," Biomed. Opt. Express **9**, 2130 (2018).
10. A. Matlock and L. Tian, "High-throughput, volumetric quantitative phase imaging with multiplexed intensity diffraction tomography," Biomed. Opt. Express **10**, 6432 (2019).
11. L. Tian and L. Waller, "3d intensity and phase imaging from light field measurements in an LED array microscope," Optica **2**, 104 (2015).
12. P. Li, D. J. Batey, T. B. Edo, and J. M. Rodenburg, "Separation of three-dimensional scattering effects in tilt-series fourier ptychography," Ultramicroscopy **158**, 1–7 (2015).
13. S. Chowdhury, M. Chen, R. Eckert, D. Ren, F. Wu, N. Repina, and L. Waller, "High-resolution 3d refractive index microscopy of multiple-scattering samples from intensity images," Optica **6**, 1211 (2019).
14. T.-A. Pham, E. Soubies, A. Goy, J. Lim, F. Soulez, D. Psaltis, and M. Unser, "Versatile reconstruction framework for diffraction tomography with intensity measurements and multiple scattering," Opt. Express **26**, 2749 (2018).
15. V. Lauer, "New approach to optical diffraction tomography yielding a vector equation of diffraction tomography and a novel tomographic microscope," J. Microsc. **205**, 165–176 (2002).
16. Y. Sung, W. Choi, C. Fang-Yen, K. Badizadegan, R. R. Dasari, and M. S. Feld, "Optical diffraction tomography for high resolution live cell imaging," Opt. Express **17**, 266 (2009).
17. S. Vertu, J.-J. Delaunay, I. Yamada, and O. Haeberlé, "Diffraction microtomography with sample rotation: influence of a missing apple core in the recorded frequency space," Open Phys. **7** (2009).
18. D. Zhang, M. N. Slipchenko, D. E. Leaird, A. M. Weiner, and J.-X. Cheng, "Spectrally modulated stimulated raman scattering imaging with an angle-to-wavelength pulse shaper," Opt. Express **21**, 13864 (2013).

19. A. Dubois, L. Vabre, A.-C. Boccara, and E. Beaurepaire, "High-resolution full-field optical coherence tomography with a linnik microscope," Appl. Opt. **41**, 805 (2002).
20. A. Sentenac and J. Mertz, "Unified description of three-dimensional optical diffraction microscopy: from transmission microscopy to optical coherence tomography: tutorial," J. Opt. Soc. Am. A **35**, 748 (2018).
21. H. Rigneault and P. Berto, "Tutorial: Coherent raman light matter interaction processes," APL Photonics **3**, 091101 (2018).
22. S. Heuke, K. Unger, S. Khadir, K. Belkebir, P. C. Chaumet, H. Rigneault, and A. Sentenac, "Coherent anti-stokes raman fourier ptychography," Opt. Express **27**, 23497 (2019).
23. P. Berto, D. Gachet, P. Bon, S. Monneret, and H. Rigneault, "Wide-field vibrational phase imaging," Phys. Rev. Lett. **109** (2012).
24. C. Heinrich, S. Bernet, and M. Ritsch-Marte, "Wide-field coherent anti-stokes raman scattering microscopy," Appl. Phys. Lett. **84**, 816–818 (2004).
25. I. Toytman, D. Simanovskii, and D. Palanker, "On illumination schemes for wide-field CARS microscopy," Opt. Express **17**, 7339 (2009).
26. I. Toytman, K. Cohn, T. Smith, D. Simanovskii, and D. Palanker, "Wide-field coherent anti-stokes raman scattering microscopy with non-phase-matching illumination," Opt. Lett. **32**, 1941 (2007).
27. S. Khadir, P. C. Chaumet, G. Baffou, and A. Sentenac, "Quantitative model of the image of a radiating dipole through a microscope," J. Opt. Soc. Am. A **36**, 478 (2019).
28. J.-X. Cheng and X. S. Xie, eds., *Coherent Raman Scattering Microscopy (Series in Cellular and Clinical Imaging)* (CRC, 2013).
29. R. Horstmeyer, R. Heintzmann, G. Popescu, L. Waller, and C. Yang, "Standardizing the resolution claims for coherent microscopy," Nat. Photonics **10**, 68–71 (2016).